Supporting Information for "Homeostatic Enhancement of Sensory Transduction"

Andrew R. Milewski, Dáibhid Ó Maoiléidigh, Joshua D. Salvi, and A. J. Hudspeth

Howard Hughes Medical Institute and Laboratory of Sensory Neuroscience, The Rockefeller University, 1230 York Avenue, New York, New York, 10065, USA

SI Appendix 1: Experimental Localization of a Hopf Bifurcation

Hartigans' dip statistic was employed to experimentally identify the stiffness value at which a supercritical Hopf bifurcation occurred in an actual hair bundle (1-3). The position distribution for a quiescent bundle is unimodal, whereas a spontaneously oscillating bundle yields a multimodal distribution. Larger values of the dip statistic arise from multimodal distributions; unimodal distributions possess smaller values. The transition from unimodal to multimodal, which occurs when the dip statistic reaches a statistically significant value, signals a bifurcation. Setting the p-value threshold at 0.01 yielded statistically significant dip values, and thus indicated spontaneous oscillations, for stiffnesses less than 710 μN·m^{-1} (Figure S1).

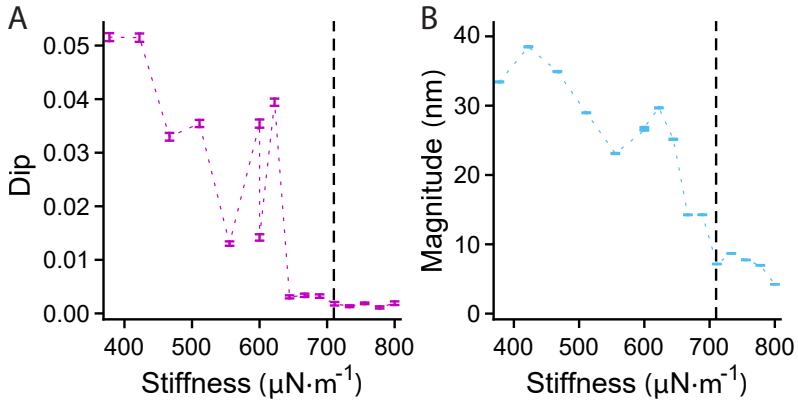

Figure S1. Experimental localization of a supercritical Hopf bifurcation in an actual hair bundle. (*A*) To the left of the dashed line at 710 μN·m^{-1} the hair bundle oscillates spontaneously. (*B*) The dependence of a hair bundle's root-mean-square magnitude of oscillation on load stiffness. In qualitative agreement with the behavior expected in the vicinity of a supercritical Hopf bifurcation, the bundle's movement rises as its operating point is poised deeper within the oscillatory region. Each data point represents the average over a 10 s interval. Error bars were acquired using 1000 bootstrap repetitions.

SI Appendix 2: Hopf Bifurcation Curves without Homeostasis

A two-dimensional dynamical system exhibits a Hopf bifurcation when $\mathrm{Tr}[J(\vec{a}_*)] = 0$ and $\det[J(\vec{a}_*)] > 0$, in which $J(\vec{a}_*)$ is the system's Jacobian matrix evaluated at the fixed point $\vec{a}_*$. Steady-state values of variables are indicated by a superscript or subscript asterisk $*$ (4). Letting $T_n = \mathrm{Tr}[J(\vec{a}_*)^n]$, these conditions

can also be expressed as $T_1 = 0$ and $T_2 < 0$. For Model I without homeostasis, a curve of Hopf bifurcations is given by (5)

$$F_{c,\mathrm{H}\pm}(k) = \pm\left[(k - a(1-b))\left(\frac{a-\alpha-k}{3(1-b)^2}\right)^{1/2} + (1-b)^3\left(\frac{a-\alpha-k}{3(1-b)^2}\right)^{3/2}\right], \tag{1}$$

when

$$k > \frac{\alpha}{b}(1-b). \tag{2}$$

Adjusting the adaptation rate α changes the size of the oscillatory region (Figure S2A).

$F_{c,\mathrm{H}\pm}(k)$ crosses the $F_c = 0$ axis at $k = (1-b)(2a+\alpha)/(2+b)$ and at $k = a - \alpha$. The area enclosed by $F_{c,\mathrm{H}\pm}(k)$ between these intersection points is

$$\begin{aligned}\mathrm{Area}_i(\alpha, b) &= 2\int_{(1-b)(2a+\alpha)/(2+b)}^{a-\alpha} F_{c,\mathrm{H}+}(k)\,dk \\ &= \frac{8(ab-\alpha)^{5/2}}{5|1-b|(2+b)^{3/2}}.\end{aligned} \tag{3}$$

From the above expression we see that the Hopf bifurcation curve forms a closed loop when $\alpha < ab$; when $\alpha = ab$ the endpoints of the integration interval coincide, and when $\alpha > ab$ the real parts of $F_{c,\mathrm{H}\pm}(k)$ intersect the $F_c = 0$ axis only at $k = (1-b)(2a+\alpha)/(2+b)$. Equation (3) quantifies how changing the adaptation rate α or strength b affects the size of the oscillatory region (Figure S2B). As long as the underdamped region does not become too small (Supplemental Material S5), the area enclosed by a contour of constant peak sensitivity increases monotonically as the oscillatory region grows (Figure S2C).

For Model II without homeostasis, and letting

$$k_{\mathrm{H}}(P_o^*) = \frac{1}{\delta\lambda_y}\left(P_o^*(1-P_o^*)(Dk_{\mathrm{gs}}(\lambda_x+\lambda_y) - fS\lambda_x) - \delta k_{\mathrm{es}}\lambda_x - \delta k_{\mathrm{gs}}(\lambda_x+\lambda_y)\right), \tag{4}$$

a Hopf bifurcation occurs when

$$F_{c,\mathrm{H}}(P_o^*) = \frac{1}{\delta}\ln\left[\frac{AP_o^*}{1-P_o^*}\right]\left(k_{\mathrm{gs}} - k_{\mathrm{H}}(P_o^*)\left(1+\frac{k_{\mathrm{gs}}}{k_{\mathrm{es}}}\right)\right) + k_{\mathrm{H}}(P_o^*)\left(\frac{k_{\mathrm{gs}}}{k_{\mathrm{es}}}DP_o^* - x_{\mathrm{es}} + \frac{f}{k_{\mathrm{es}}}(1-SP_o^*)\right) - k_{\mathrm{gs}}DP_o^*, \tag{5}$$

so long as

$$\lambda_x[(1-P_o^*)P_o^*(fS - Dk_{\mathrm{gs}}) + \delta(k_{\mathrm{es}}+k_{\mathrm{gs}})]^2 - \lambda_y k_{\mathrm{gs}}(D(1-P_o^*)P_o^* - \delta)[(1-P_o^*)P_o^*(fS - Dk_{\mathrm{gs}}) + \delta k_{\mathrm{gs}}] < 0. \tag{6}$$

In the above equations, P_o^* is the steady-state channel open probability. Given a point (k, F_c) in the state diagram and values for all the other parameters, P_o^* can be found by solving the following equation

numerically:

$$F_c = \frac{1}{\delta}\ln\left[\frac{AP_o^*}{1-P_o^*}\right]\left(k_{\rm gs} - k\left(1+\frac{k_{\rm gs}}{k_{\rm es}}\right)\right) + k\left(\frac{k_{\rm gs}}{k_{\rm es}}DP_o^* - x_{\rm es} + \frac{f}{k_{\rm es}}(1-SP_o^*)\right) - k_{\rm gs}DP_o^*. \quad (7)$$

Alternatively, P_o^* at the Hopf bifurcation can be found from equation (4):

$$P_{o,\rm H\pm}^*(k) = \frac{1}{2}\left[1 \pm \sqrt{\frac{(Dk_{\rm gs}-4\delta)(\lambda_x+\lambda_y) - fS\lambda_x - 4\delta(k_{\rm es}\lambda_x+\lambda_y k)}{Dk_{\rm gs}(\lambda_x+\lambda_y)-fS\lambda_x}}\right]. \quad (8)$$

Using $P_{o,\rm H\pm}^*(k)$, it is possible to express the Hopf bifurcation curve in terms of the two functions

$$F_{c,\rm H1}(k) = \frac{1}{\delta}\ln\left[\frac{AP_{o,\rm H+}^*(k)}{1-P_{o,\rm H+}^*(k)}\right]\left(k_{\rm gs} - k\left(1+\frac{k_{\rm gs}}{k_{\rm es}}\right)\right) + k\left(\frac{k_{\rm gs}}{k_{\rm es}}DP_{o,\rm H+}^*(k) - x_{\rm es} + \frac{f}{k_{\rm es}}(1-SP_{o,\rm H+}^*(k))\right) - k_{\rm gs}DP_{o,\rm H+}^*(k), \quad (9)$$

$$F_{c,\rm H2}(k) = \frac{1}{\delta}\ln\left[\frac{AP_{o,\rm H-}^*(k)}{1-P_{o,\rm H-}^*(k)}\right]\left(k_{\rm gs} - k\left(1+\frac{k_{\rm gs}}{k_{\rm es}}\right)\right) + k\left(\frac{k_{\rm gs}}{k_{\rm es}}DP_{o,\rm H-}^*(k) - x_{\rm es} + \frac{f}{k_{\rm es}}(1-SP_{o,\rm H-}^*(k))\right) - k_{\rm gs}DP_{o,\rm H-}^*(k). \quad (10)$$

Adjusting the adaptation-motor strength f changes the location and size of the self-oscillation region (Figure 2SD).

There are lines of saddle-node bifurcations that are not shown in Figures 1-3 of the main text or in Figures S2-S4, but are discussed in SI8. These bifurcations give rise to multiple fixed points so that a bistable region, for which there are two stable fixed points, exists in the bundle's state diagram near where the Hopf bifurcation curve crosses itself (Figures S6-S8). This crossing does not signify a higher-order bifurcation, but rather indicates Hopf bifurcations in two separate fixed points that happen to occur at the same operating points. As discussed above, the location of the Hopf bifurcation curve's crossing depends on parameter values. Higher-order bifurcations are present near this crossing point and are discussed elsewhere (5).

The functions $F_{c,\rm H1}(k)$ and $F_{c,\rm H2}(k)$ intersect at two values of k. One value, which bounds the region of spontaneous oscillations on the right, is

$$k_{\rm R} = \frac{k_{\rm gs}(\lambda_x+\lambda_y)(D-4\delta) - \lambda_x(fS+4k_{\rm es}\delta)}{4\delta\lambda_y}. \quad (11)$$

The second value, $k_{\rm L}$, which bounds the region of spontaneous oscillations on the left, can be found numerically. The area enclosed by the Hopf bifurcation loop can then be calculated numerically from the integral

$$\text{Area}_{ii}(f,S) = \int_{k_{\rm L}}^{k_{\rm R}} \left[F_{c,\rm H1}(k,f,S) - F_{c,\rm H2}(k,f,S)\right] dk. \quad (12)$$

Note that $F_{c,\rm H1}(k,f,S) \geq F_{c,\rm H2}(k,f,S)$ on the interval $k \in [k_{\rm L}, k_{\rm R}]$. Changing the adaptation-motor strength f or efficacy of Ca^{2+} inhibition S affects the size and location of the oscillatory region (Figure S2E). As

the size of the oscillatory region grows, the area enclosed by a curve of constant peak sensitivity increases (Figure S2F), as long as the underdamped region does not become too small (Supplemental Material S5).

In both models, the area contained within a contour of constant peak sensitivity, quality factor, or compressive range is calculated numerically.

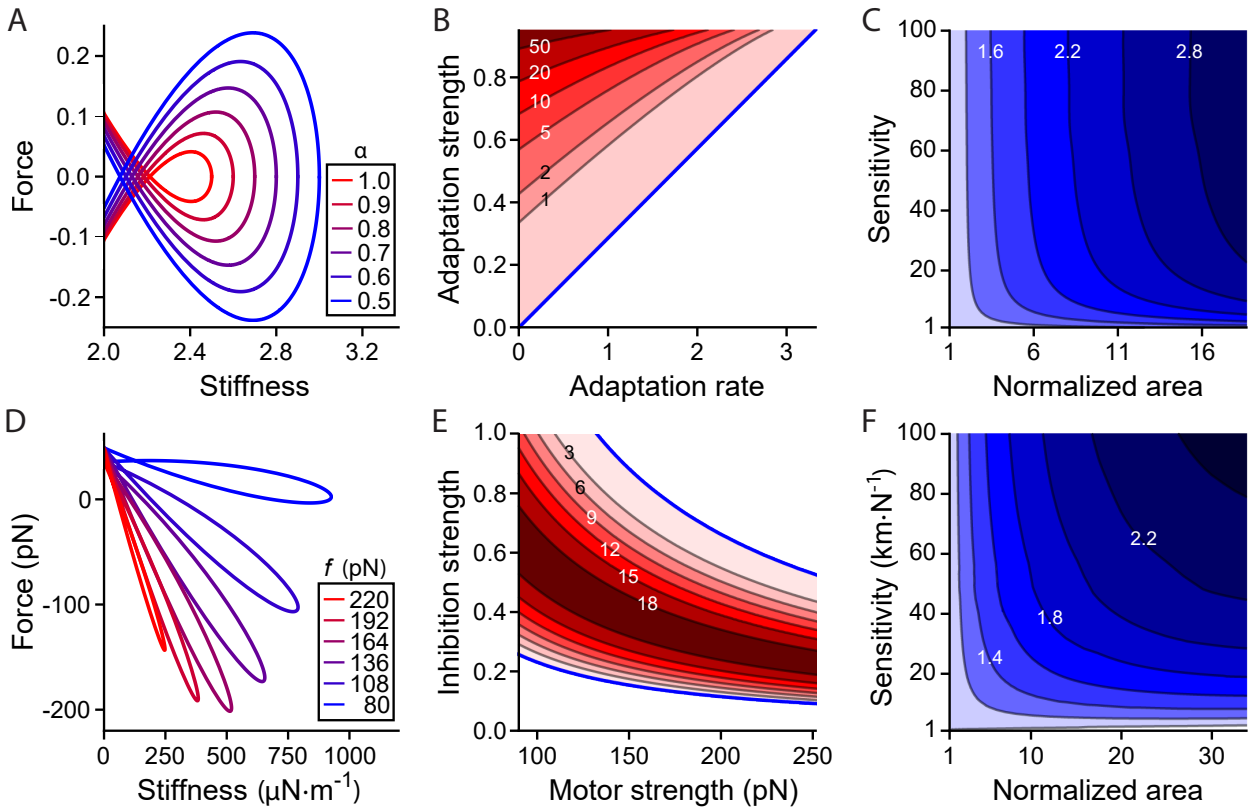

Figure S2. Hopf bifurcation curves without homeostasis. (A) Hopf bifurcation curves in the state diagram of Model I for various values of the adaptation rate α. (B) Area enclosed by the Hopf bifurcation loop as a function of adaptation strength b and adaptation rate α. Darker shades of red indicate larger areas and each contour is labeled with its area. The blue line marks where $\alpha = ab$. In the white region of the plot, for which $\alpha > ab$, the Hopf bifurcation curve does not encircle a bounded region of state space. (C) Area contained within peak-sensitivity contours relative to that contained in contours when $\alpha = 1$, as a function of the peak sensitivity and of the normalized area of the oscillatory region, $\mathrm{Area}_i(\alpha, b)/\mathrm{Area}_i(1, b)$. α ranges from 1.0, at a normalized area of 1, to 0.5 at the maximum normalized area shown. Darker shades of blue indicate larger areal ratios. (D) Hopf bifurcation curves in Model II for various values of the adaptation-force strength f. (E) Area enclosed by the Hopf bifurcation loop as a function of motor strength f and of the strength of Ca^{2+}-mediated inhibition S. Darker shades of red indicate larger areas and each contour is labeled with its area in units of $10^{-15}\,\mathrm{N}^2{\cdot}\mathrm{m}^{-1}$. The Hopf bifurcation curve does not enclose a bounded region for values located in the white region of the plot. As f increases from 80 pN, the area of the oscillatory region initially increases to a maximum and then decreases for large enough values of f. (F) Area contained within peak-sensitivity contours relative to that contained in the contours when $f = 250$ pN, as a function of the peak sensitivity and of the normalized area of the oscillatory region, $\mathrm{Area}_{ii}(f, S)/\mathrm{Area}_{ii}(250pN, S)$. f ranges from 250 pN at a normalized area of 1 to 180 pN at the maximum normalized area shown. The calculations in panels C and F exclude the area of the self-oscillation region. All parameter values are listed in Tables S1 and S2.

SI Appendix 3: Hopf Bifurcation Curves with Homeostasis

Hopf bifurcations occur in a three-dimensional dynamical system when

$$T_3 = T_1^3 \qquad \text{and} \qquad T_2 < T_1^2. \tag{13}$$

In Model I, when the steady-state adaptation rate α^* exceeds zero, the system's fixed points are given by

$$\alpha_* > 0 \Rightarrow \begin{cases} f_* = b\, x_* \\ \alpha_* = \alpha_0 - \beta_\alpha x_*^2 \\ F_c = k x_* - a(1-b) x_* + (1-b)^3 x_*^3. \end{cases}$$

At these fixed points, a Hopf bifurcation occurs when

$$F_{c,\mathrm{H}\pm}(k) = \pm \left[(k - a(1-b)) \left(\frac{a - \alpha_0 - k}{3(1-b)^2 - \beta_\alpha} \right)^{1/2} + (1-b)^3 \left(\frac{a - \alpha_0 - k}{3(1-b)^2 - \beta_\alpha} \right)^{3/2} \right] \tag{14}$$

and when

$$k > \frac{3\alpha_0(1-b)^3 - a\beta_\alpha(1-b)}{3b(1-b)^2 - \beta_\alpha}. \tag{15}$$

Note that setting $\beta_\alpha = 0$ reproduces Eqs. (1) and (2). Adjusting the homeostasis strength β_α shifts the position and size of the Hopf bifurcation curve; $\beta_\alpha = 0$ corresponds to inactive homeostasis (Figure S3*A*).

The values of the parameters a, b, α_0, τ_α, and β_α need to be determined, a choice guided by the effect that each parameter has on the self-oscillation region. The Hopf bifurcation curve, $F_{c,\mathrm{H}}(k)$, crosses $F_c = 0$ at

$$[k_0] = \left\{ \frac{(1-b)^3(2a + \alpha_0) - a(1-b)\beta_\alpha}{2 - 3b + b^3 - \beta_\alpha}, a - \alpha_0 \right\}.$$

The area of the region of spontaneous oscillation is then

$$\begin{aligned} \mathrm{Area}_{\mathrm{I}}(b, \beta_\alpha) &= 2 \int_{[k_0]_1}^{[k_0]_2} F_{c,\mathrm{H}+}(k)\, dk \\ &= \frac{8}{15} |3(1-b)^2 - \beta_\alpha| \frac{(ab - \alpha_0)^{5/2}}{(2 - 3b + b^3 - \beta_\alpha)^{3/2}}. \end{aligned} \tag{16}$$

The above expression is valid only if $b > \alpha_0/a$ and $\beta_\alpha < \alpha_0(2+b)(1-b)^2/(ab)$. If $b = \alpha_0/a$, then $[k_0]_1 = [k_0]_2$ and a Hopf bifurcation loop does not exist at smaller values of b. At $\beta_\alpha = \alpha_0(2+b)(1-b)^2/(ab)$, $[k_0]_1$ collides with two Bogdanov-Takens points, and the Hopf bifurcation does not form a closed loop when $\beta_\alpha > \alpha_0(2+b)(1-b)^2/(ab)$. Dividing $\mathrm{Area}_{\mathrm{I}}(b, \beta_\alpha)$ by $\mathrm{Area}_{\mathrm{I}}(b, 0)$, the area of the oscillatory region when the homeostatic mechanism is inactive, yields the dilation factor, or relative increase in area effected by setting

the homeostasis parameter to β_α:

$$\frac{\text{Area}_{\text{I}}(b,\beta_\alpha)}{\text{Area}_{\text{I}}(b,0)} = \frac{|3(1-b)^2-\beta_\alpha|(2-3b+b^3)^{3/2}}{3(1-b)^2(2-3b+b^3-\beta_\alpha)^{3/2}}. \tag{17}$$

The dilation factor depends on only the parameters b and β_α and is independent of a, α_0, and τ_α. Therefore, a was set to 3.5 (5), α_0 was set to 1 for simplicity, and τ_α was set to 1000 to ensure separation between the timescale governing the homeostatic mechanism and the other timescales present in the system: homeostasis was assumed to be a relatively slow process.

The dilation factor depends on the parameters b and β_α, the adaptation strength and homeostasis strength respectively (Figure S3B). The value of b was set to 0.35 and that of β_α to 3/4. This choice of values for b and β_α yields a dilation factor greater than three. Although greater dilation factors are possible, the values selected render the increase in area robust to variations in b or β_α. We note, however, that the specified parameter values do not optimize the dilation factor or its robustness to changes in parameter values. In this work we avoid optimization to illustrate that a biological system might not need to exert tight control over parameter values to achieve its performance specifications. A summary of the parameter values used in Model I is given in Table S1.

Table S1: Parameter Values in Model I

a	3.5	b	0.35	τ_α	10^3
α_0	1	$^*\beta_\alpha$	0.75		

$^*\beta_\alpha = 0$ when homeostasis is off

Larger dilation factors effect greater areal ratios for the peak sensitivity (Figure S3C).

For Model II, fixed points are found from

$$\begin{cases} f_* = f_0 - \beta_f P_o^* \\ k_{\text{es}} y_* = k_{\text{gs}}\left(\frac{1}{\delta}\ln\left[\frac{AP_o^*}{1-P_o^*}\right] - DP_o^*\right) + k_{\text{es}}x_{\text{es}} - (f_0-\beta_f P_o^*)(1-SP_o^*) \\ kx_* = F_c - k_{\text{gs}}\left(\frac{1}{\delta}\ln\left[\frac{AP_o^*}{1-P_o^*}\right] - DP_o^*\right), \end{cases}$$

$$x_* = y_* + \frac{1}{\delta}\ln\left[\frac{AP_o^*}{1-P_o^*}\right],$$

$$\Rightarrow F_c = \frac{1}{\delta}\ln\left[\frac{AP_o^*}{1-P_o^*}\right]\left(k_{\text{gs}} - k\left(1+\frac{k_{\text{gs}}}{k_{\text{es}}}\right)\right) + k\left(\frac{k_{\text{gs}}}{k_{\text{es}}}DP_o^* - x_{\text{es}} + \frac{1}{k_{\text{es}}}(f_0-\beta_f P_o^*)(1-SP_o^*)\right) - k_{\text{gs}}DP_o^*. \tag{18}$$

Given a point (k, F_c) in state space and values for all the other parameters, Eq. (18) can be solved numerically for P_o^*, and $f_* = f_0 - \beta_f P_o^*$ then follows.

A Hopf bifurcation occurs for Model II when

$$F_{c,\mathrm{H}}(P_o^*) = \frac{1}{\delta}\ln\left[\frac{AP_o^*}{1-P_o^*}\right]\left(k_{\mathrm{gs}} - k_{\mathrm{H}}(P_o^*)\left(1+\frac{k_{\mathrm{gs}}}{k_{\mathrm{es}}}\right)\right) + k_{\mathrm{H}}(P_o^*)\left(\frac{k_{\mathrm{gs}}}{k_{\mathrm{es}}}DP_o^* - x_{\mathrm{es}} + \frac{1}{k_{\mathrm{es}}}(f_0 - \beta_f P_o^*)(1-SP_o^*)\right) - k_{\mathrm{gs}}DP_o^*, \tag{19}$$

in which

$$k_{\mathrm{H}}(P_o^*) = -\frac{1}{2}\left(c_1 - \sqrt{c_1^2 - 4c_2}\right), \tag{20}$$

$$\begin{aligned} c_1 = \big\{&\tau_f^2\widehat{P}^2(Dk_{\mathrm{gs}} - f_0S + \beta_f P_o^* S)[S\lambda_x(\beta_f P_o^* - f_0) + Dk_{\mathrm{gs}}\lambda_T] + \delta^2[k_{\mathrm{gs}}\lambda_y\tau_f(2\lambda_y + 2k_{\mathrm{es}}\tau_f + k_{\mathrm{gs}}\tau_f) + \lambda_x(\lambda_y + \tau_f k_{\mathrm{es}} + \tau_f k_{\mathrm{gs}})^2] \\ &+\tau_f\widehat{P}\delta\big(S(f_0 - \beta_f P0)[k_{\mathrm{gs}}\lambda_y\tau_f + 2\lambda_x(\lambda_y + \tau_f k_{\mathrm{es}} + \tau_f k_{\mathrm{gs}})] - 2Dk_{\mathrm{gs}}\lambda_T[\lambda_y + \tau_f(k_{\mathrm{es}} + k_{\mathrm{gs}})]\big)\big\}\Big/ \\ &\big(\delta\lambda_y\tau_f[\tau_f\widehat{P}(f_0S + \beta_f P_o^* S - Dk_{\mathrm{gs}}) + \delta\lambda_y + \tau_f\delta(k_{\mathrm{es}} + k_{\mathrm{gs}})]\big), \end{aligned}$$

$$\begin{aligned} c_2 = \big\{&\lambda_x^2\tau_f\beta_f^2\widehat{P}^2P_o^*S(2P_o^*S-1) + \beta_f\lambda_x\widehat{P}\big(\lambda_x\lambda_y\delta(1-2P_o^*S) - \tau_f(3P_o^*S-1)[\widehat{P}(f_0S\lambda_x - Dk_{\mathrm{gs}}\lambda_T) + k_{\mathrm{es}}\lambda_x\delta + k_{\mathrm{gs}}\lambda_T\delta] - \tau_f^2k_{\mathrm{es}}k_{\mathrm{gs}}P_o^*S[\delta + D\widehat{P}]\big) \\ &+\big(\widehat{P}[f_0S\lambda_x - Dk_{\mathrm{gs}}\lambda_T] + k_{\mathrm{gs}}\lambda_T\delta + k_{\mathrm{es}}\lambda_x\delta\big)\big(\tau_f\widehat{P}[f_0S\lambda_x - Dk_{\mathrm{gs}}(\lambda_T + k_{\mathrm{es}}\tau_f)] + \delta[k_{\mathrm{gs}}\tau_f(\lambda_T + \tau_f k_{\mathrm{es}}) + \lambda_x(\lambda_y + \tau_f k_{\mathrm{es}})]\big)\big\}\Big/ \\ &\big(\delta\lambda_y\tau_f[\tau_f\widehat{P}(f_0S + \beta_f P_o^* S - Dk_{\mathrm{gs}}) + \delta\lambda_y + \tau_f\delta(k_{\mathrm{es}} + k_{\mathrm{gs}})]\big), \end{aligned}$$

$$\widehat{P} = P_o^*(1-P_o^*), \text{ and } \lambda_T = \lambda_x + \lambda_y,$$

as long as

$$k_{\mathrm{H}}(P_o^*) > \frac{P_o^*(1-P_o^*)[Dk_{\mathrm{gs}}(\lambda_x + \lambda_y + k_{\mathrm{es}}\tau_f) - f_0S\lambda_x + \beta_f(1-2P_o^*S)\lambda_x] - k_{\mathrm{gs}}\delta(\lambda_x + \lambda_y) - k_{\mathrm{es}}\delta(\lambda_x + k_{\mathrm{gs}}\tau_f)}{\tau_f P_o^*(1-P_o^*)(f_0S - Dk_{\mathrm{gs}} - \beta_f P_o^* S) + \lambda_y\delta + \tau_f\delta(k_{\mathrm{es}} + k_{\mathrm{gs}})}. \tag{21}$$

Setting $\beta_f = 0$ reproduces the parametric curve $\left(k_{\mathrm{H}}(P_o^*), F_{c,\mathrm{H}}(P_o^*)\right)$ found in the absence of homeostasis. Changing the homeostasis strength β_f shifts the position and size of the Hopf bifurcation curve (Figure S3*D*).

Values for the parameters k_{gs}, k_{es}, δ, D, N, A, T, ΔG, and x_{es} were taken from (5) or (6) and are based on biophysical measurements or estimates of hair bundle parameters in sacculi of American bullfrogs. The value for S was chosen to ensure the existence of a region of spontaneous oscillation for a broad range of myosin-motor strengths f (Figure S2*E*). Values for λ_x and λ_y were chosen to ensure that the maximum frequency of spontaneous oscillations was less than 200 Hz. Choices for the remaining parameters, f_0 and β_f, are described below.

When $\beta_f \neq 0$ it is not possible to express the parametric curve $\left(k_{\mathrm{H}}(P_o^*), F_{c,\mathrm{H}}(P_o*)\right)$ in terms of a set of elementary functions. Therefore, the parametric equations, $k_{\mathrm{H}}(P_o^*)$ and $F_{c,\mathrm{H}}(P_o*)$, and Stokes's theorem were used to calculate the area enclosed by the Hopf bifurcation loop for various values of f_0 and β_f. Let $\vec{U}$ be a vector field with $\vec{\nabla}\times\vec{U}$ a unit vector field perpendicular to the surface Σ. Stoke's theorem then states that

$$\oint_{\partial\Sigma}\vec{U}\cdot d\vec{r} = \iint_{\Sigma}\vec{\nabla}\times\vec{U}\cdot d\vec{\Sigma} = \Sigma,$$

in which $\partial\Sigma$ is the boundary curve of Σ with the normal vector field $d\vec{\Sigma}$ and $\vec{r}$ is a parameterization of $\partial\Sigma$. The Hopf bifurcation curve is given by:

$$\vec{r} = \Big(k_{\mathrm{H}}(P_o^*, f_0, \beta_f), F_{c,\mathrm{H}}(P_o^*, f_0, \beta_f), 0\Big),$$

in which P_o^* is a variable and f_0 and β_f are parameters. The differential tangent-vector field along the curve $\vec{r}$ is then

$$d\vec{r} = \frac{\partial}{\partial P_o^*}\Big(k_{\mathrm{H}}(P_o^*, f_0, \beta_f), F_{c,\mathrm{H}}(P_o^*, f_0, \beta_f), 0\Big)\, dP_o^*,$$

meaning the area of a surface Σ can be found by line integration around the boundary of Σ. We can use various vector fields, $\vec{U}$, in our line integral. Two simple examples are

$$\vec{U} = \Big(0, k_{\mathrm{H}}(P_o^*, f_0, \beta_f), 0\Big) \;\text{ or }\; \vec{U} = \Big(-F_{c,\mathrm{H}}(P_o^*, f_0, \beta_f), 0, 0\Big).$$

The area enclosed by the Hopf bifurcation loop is then given by

$$\mathrm{Area}_{\,\mathrm{II}}(f_0, \beta_f) = \int_{[P_o^*]_1}^{[P_o^*]_2} k_{\mathrm{H}}(P_o^*, f_0, \beta_f) \frac{\partial}{\partial P_o^*} F_{c,\mathrm{H}}(P_o^*, f_0, \beta_f)\, dP_o^* \tag{22}$$

$$\text{or}\;\; \mathrm{Area}_{\,\mathrm{II}}(f_0, \beta_f) = -\int_{[P_o^*]_1}^{[P_o^*]_2} F_{c,\mathrm{H}}(P_o^*, f_0, \beta_f) \frac{\partial}{\partial P_o^*} k_{\mathrm{H}}(P_o^*, f_0, \beta_f)\, dP_o^*, \tag{23}$$

in which $[P_o^*]_1$ and $[P_o^*]_2$ are the values of the parameter P_o^* where the Hopf bifurcation curve crosses itself. These values are found numerically. Three fixed points exist at this intersection, two of which, corresponding to $[P_o^*]_1$ and $[P_o^*]_2$, are stable. As P_o^* is increased from $[P_o^*]_1$, the bundle crosses a saddle-node bifurcation, beyond which the fixed point associated with $[P_o^*]_1$ persists whereas the fixed point associated with $[P_o^*]_2$ vanishes. As P_o^* is increased further toward $[P_o^*]_2$, the remaining stable fixed point shifts continuously toward the fixed point originally associated with $[P_o^*]_2$. When P_o^* nears $[P_o^*]_2$, the bundle again crosses a saddle-node bifurcation, at which point the fixed point originally associated with $[P_o^*]_1$ materializes. Integrating along the Hopf bifurcation curve from $[P_o^*]_1$ to $[P_o^*]_2$ tracks the bundle's position as it transitions smoothly from the $[P_o^*]_1$ fixed point to the $[P_o^*]_2$ fixed point.

The dilation factor of the self-oscillation region,

$$\frac{\mathrm{Area}_{\,\mathrm{II}}(f_0, \beta_f)}{\mathrm{Area}_{\,\mathrm{II}}(f_0, 0)}, \tag{24}$$

depends on the homeostasis strength β_f and on the adaptation-motor strength f_0 in the absence of homeostasis (Figure S3*E*). The value of f_0 was chosen to be 220 pN and β_f was set to 110 pN. This choice of

parameter values results in a more than tenfold dilation factor while striking a balance with the robustness of this dilation factor to changes in f_0 or β_f. Once again, the parameter values were not optimized; other choices would yield a larger dilation factor as well as render this increase more robust to changes in f_0 and β_f. Unless otherwise stated, Table S2 gives the parameter values used in Model II. Increases in the dilation factor yield larger peak-sensitivity areal ratios (Figure S3F). We conclude that increasing the size of the oscillatory region enhances the robustness of the bundle's ability to detect signals, as long as the underdamped region is not made too small (Supplemental Material S5).

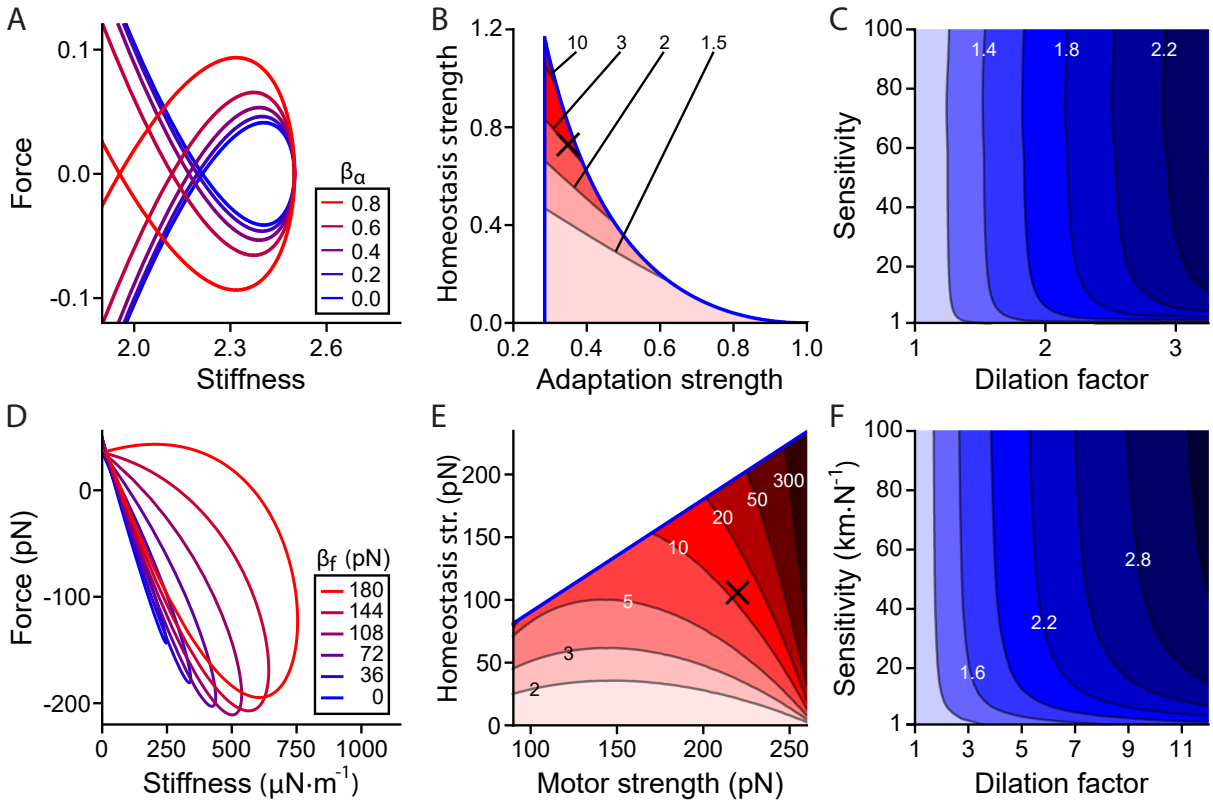

Figure S3. Hopf bifurcation curves with homeostasis. (A) Hopf bifurcation curves in the state diagram of Model I for various values of homeostatic strength β_α. (B) Dilation factor, Eq. (17), as a function of the strength of adaptation b and homeostasis strength β_α. Darker shades of red indicate larger dilation factors. The $\times$ symbol marks the chosen values of $b = 0.35$ and $\beta_\alpha = 0.75$. The blue curves bound the set of values at which a closed Hopf bifurcation loop exists. (C) Peak-sensitivity areal ratios as a function of the peak sensitivity and of the oscillatory region's dilation factor. Darker shades of blue indicate larger areal ratios. β_α ranges from 0 at a dilation factor of 1 to 0.75 at the maximum dilation factor shown. (D) Hopf bifurcation curves in the state diagram of Model II for various values of β_f. (E) Dilation factor, Eq. (24), as a function of the baseline motor strength f_0 and homeostasis strength β_f. Darker shades of red indicate larger dilation factors. The region encircled by a Hopf bifurcation curve is bounded at all values shown. The chosen values for $f_0 = 220$ pN and $\beta_f = 110$ pN are marked by the $\times$ symbol. (F) Peak-sensitivity areal ratios as a function of the peak sensitivity and of the oscillatory region's dilation factor. Darker shades of blue indicate larger areal ratios. β_f ranges from 0 at a dilation factor of 1 to 110 pN at the maximum dilation factor shown. The areal ratio calculations in panels C and F exclude the area of the self-oscillation region. Parameter values are listed in Tables S1 and S2.

Table S2: Parameter Values in Model II

k_{gs}	816	μN·m^{-1}	k_{es}	150	μN·m^{-1}
λ_x	500	nN·s·m^{-1}	λ_y	2500	nN·s·m^{-1}
* δ	5.16	nm	D	49	nm
† A	2.53		S	0.5	
N	50		T	295	K
ΔG	10	k_BT	k_B	1.4×10^{-23}	J·K^{-1}
x_{es}	0	m	τ_f	0.2	s
‡ β_f	110	pN	f_0	220	pN

* $\delta = Nk_BT/(Dk_{\mathrm{gs}})$

† $A = \exp[(\Delta G + k_{\mathrm{gs}}D^2)/(2Nk_BT)]$

‡ $\beta_f = 0$ when homeostasis is off

SI Appendix 4: Linear Sensitivity and Quality Factor

In Model I, the peak sensitivity of the linearized system is

$$|\chi_0(\omega_R)| = \left|\frac{\alpha_* + i\omega_R}{\alpha_*\widehat{a}\,b + (\alpha_* + i\omega_R)(k - \widehat{a} + i\omega_R)}\right|, \text{ or}$$

$$|\chi_0(\omega_R)| = \sqrt{\frac{\alpha_*^2 + \omega_R^2}{\omega_R^4 + \omega_R^2[k^2 + \alpha_*^2 - 2\widehat{a}(k + \alpha_* b) + \widehat{a}^2] + \alpha_*^2[k - \widehat{a}(1-b)]^2}}\,, \tag{25}$$

in which $\alpha_* = \alpha_0 - \beta_\alpha x_*^2$, $\widehat{a} = a - 3(1-b)^2x_*^2$, and the resonant frequency ω_R is

$$\omega_R = \sqrt{-\alpha_*^2 + \sqrt{\widehat{a}\,b[\widehat{a}(b-2) + 2(k+\alpha_*)]\alpha_*^2}}\,. \tag{26}$$

The quality factor Q is given by $\omega_R/(\omega_+ - \omega_-)$, in which $\omega_\pm$ is found by solving $\left|\chi_0(\omega_\pm)\right| = \left|\chi_0(\omega_R)\right|/\sqrt{2}$ for $\omega_\pm$

$$\omega_\pm = \sqrt{\frac{2 - (\widehat{a}-k)^2 + 2\alpha_*\widehat{a}b - \alpha_*^2 \pm \sqrt{[2-(\widehat{a}-k)^2]^2 + 4\alpha_*\widehat{a}b[2-(\widehat{a}-k)^2] + 2[2 + (\widehat{a}-k)(\widehat{a}(4b-1)+k)]\alpha_*^2 - 4\widehat{a}b\alpha_*^3 + \alpha_*^4}}{2}}\,. \tag{27}$$

The peak sensitivity of the linearized system for Model II is given by

$$|\chi_0(\omega_R)| = \left|\frac{\widehat{\beta}_f + (k_{\mathrm{es}}\delta + \widehat{k}_{\mathrm{gs}}\delta + f_*\widehat{S} + i\omega_R\delta\lambda_y)(1 + i\omega_R\tau_f)}{(k + \widehat{k}_{\mathrm{gs}} + i\omega_R\lambda_x)[\widehat{\beta}_f + (k_{\mathrm{es}}\delta + \widehat{k}_{\mathrm{gs}}\delta + f_*\widehat{S} + i\omega_R\delta\lambda_y)(1 + i\omega_R\tau_f)] - \widehat{k}_{\mathrm{gs}}[\widehat{\beta}_f + (\widehat{k}_{\mathrm{gs}}\delta + f_*\widehat{S})(1 + i\omega_R\tau_f)]}\right|, \tag{28}$$

in which $f_* = f_0 - \beta_f P_o^*$, $\widehat{k}_{\mathrm{gs}} = k_{\mathrm{gs}}[1 - DP_o^*(1-P_o^*)/\delta]$, $\widehat{\beta}_f = \beta_f(1-P_o^*)(1-P_o^*S)P_o^*$, and $\widehat{S} = SP_o^*(1-P_o^*)$. Analytical expressions exist for ω_R, $\omega_\pm$, and Q, but are omitted here to conserve space.

SI Appendix 5: Underdamped Region

All calculations were performed within the underdamped region of the state diagram, the set of operating points at which the bundle exhibits ringing in response to small force steps. Outside the underdamped region the bundle exhibits little amplification of periodic stimuli. The boundary of the underdamped region occurs when the discriminant of the Jacobian's characteristic polynomial is equal to zero, whereupon the system is critically damped.

The boundary of the underdamped region in Model I is given by

$$k_{\mathrm{U}\pm}(x_*) = a + \alpha_0 - x_*^2[3(1-b)^2 + \beta_\alpha] \pm 2\sqrt{b[a - 3(1-b)^2 x_*^2][\alpha_0 - x_*^2\beta_\alpha]}, \tag{29}$$

$$F_{c,\mathrm{U}\pm}(x_*) = [k_{\mathrm{U}\pm}(x_*) - a(1-b)]x_* + (1-b)^3 x_*^3. \tag{30}$$

Figure S6 depicts the underdamped region for the homeostasis off ($\beta_\alpha = 0$) and on ($\beta_\alpha = 3/4$) conditions.

For Model II, when homeostasis is inactive, the boundary of the underdamped region is given by

$$k_{U\pm}(P_o^*) = \tag{31}$$
$$\frac{k_{\mathrm{gs}}[D(1-P_o^*)P_o^* - \delta](\lambda_y - \lambda_x) + \lambda_x[f_0(1-P_o^*)P_o^* S + k_{\mathrm{es}}\delta] \pm 2\sqrt{k_{\mathrm{gs}}[D(1-P_o^*)P_o^* - \delta][(1-P_o^*)P_o^*(f_0 S - Dk_{\mathrm{gs}}) + k_{\mathrm{gs}}\delta]\lambda_y\lambda_x}}{\lambda_y\delta},$$

$$F_{c,U\pm} = \frac{1}{\delta}\ln\left[\frac{AP_o^*}{1-P_o^*}\right]\left(k_{\mathrm{gs}} - k_{U\pm}(P_o^*)\left(1 + \frac{k_{\mathrm{gs}}}{k_{\mathrm{es}}}\right)\right) + k_{U\pm}(P_o^*)\left(\frac{k_{\mathrm{gs}}}{k_{\mathrm{es}}}DP_o^* - x_{\mathrm{es}} + \frac{f}{k_{\mathrm{es}}}(1 - SP_o^*)\right) - k_{\mathrm{gs}}DP_o^*. \tag{32}$$

When homeostasis is active, the expression for $k_{U\pm}(P_o^*)$ is very large, and is therefore omitted to conserve space. Curves bounding the underdamped region are shown in Figure S7.

SI Appendix 6: Trade-off between Quality Factor and Decay Time

As the sharpness of a system's frequency selectivity Q increases, so does the time needed for that system to reach a steady state. For small perturbations, the timescales of a system's response are given by the real parts of the negative reciprocals of the Jacobian matrix's eigenvalues. In Model I, the eigenvalues are $\xi_\alpha = -1/\tau_\alpha$ and

$$\xi_\pm = \frac{1}{2}\Big[a - k - \alpha_0 + x_*^2(\beta_\alpha - 3(1-b)^2) \pm \sqrt{\left(k - a + \alpha_0 + x_*^2[3(1-b)^2 - \beta_\alpha]\right)^2 - 4[k - a(1-b) + 3(1-b)^3 x_*^2](\alpha_0 - x_*^2\beta_\alpha)}\Big]. \tag{33}$$

The relevant timescales are therefore τ_α and

$$\tau = 2\left[k - a + \alpha_0 + x_*^2(3(1-b)^2 - \beta_\alpha)\right]^{-1}. \tag{34}$$

τ_α is relevant only when $\beta_\alpha \neq 0$ because stimulating the bundle does not engage the homeostatic mechanism when $\beta_\alpha = 0$.

By a similar calculation, τ for Model II when homeostasis is off is given by

$$\tau = \frac{2\delta\lambda_x\lambda_y}{f_0(1-P_o^*)P_o^* S\lambda_x + (k_{\mathrm{es}} + k_{\mathrm{gs}})\delta\lambda_x + (k + k_{\mathrm{gs}})\delta\lambda_y - Dk_{\mathrm{gs}}(1-P_o^*)P_o^*(\lambda_x + \lambda_y)}. \tag{35}$$

As for Model I, τ_f is irrelevant when homeostasis is inactive.

At operating points far from the Hopf bifurcation, the timescales τ_α and τ_f substantially exceed τ and determine the relaxation time when the bundle's displacement x is greatly perturbed (Figure 7). Small perturbations, however, do not engender great changes in the homeostatic variables α or f.

In both models, τ specifies the approximate time required for the amplitude of the bundle's response to a small perturbation to decay by a factor of $1/e$. Homeostasis increases the set of operating points at which τ exceeds a threshold (Figure S4). Therefore, the cost of enhancing the robustness of the bundle's frequency selectivity is a slowed reaction to stimuli. This cost is proportionally smaller in Model II than in Model I.

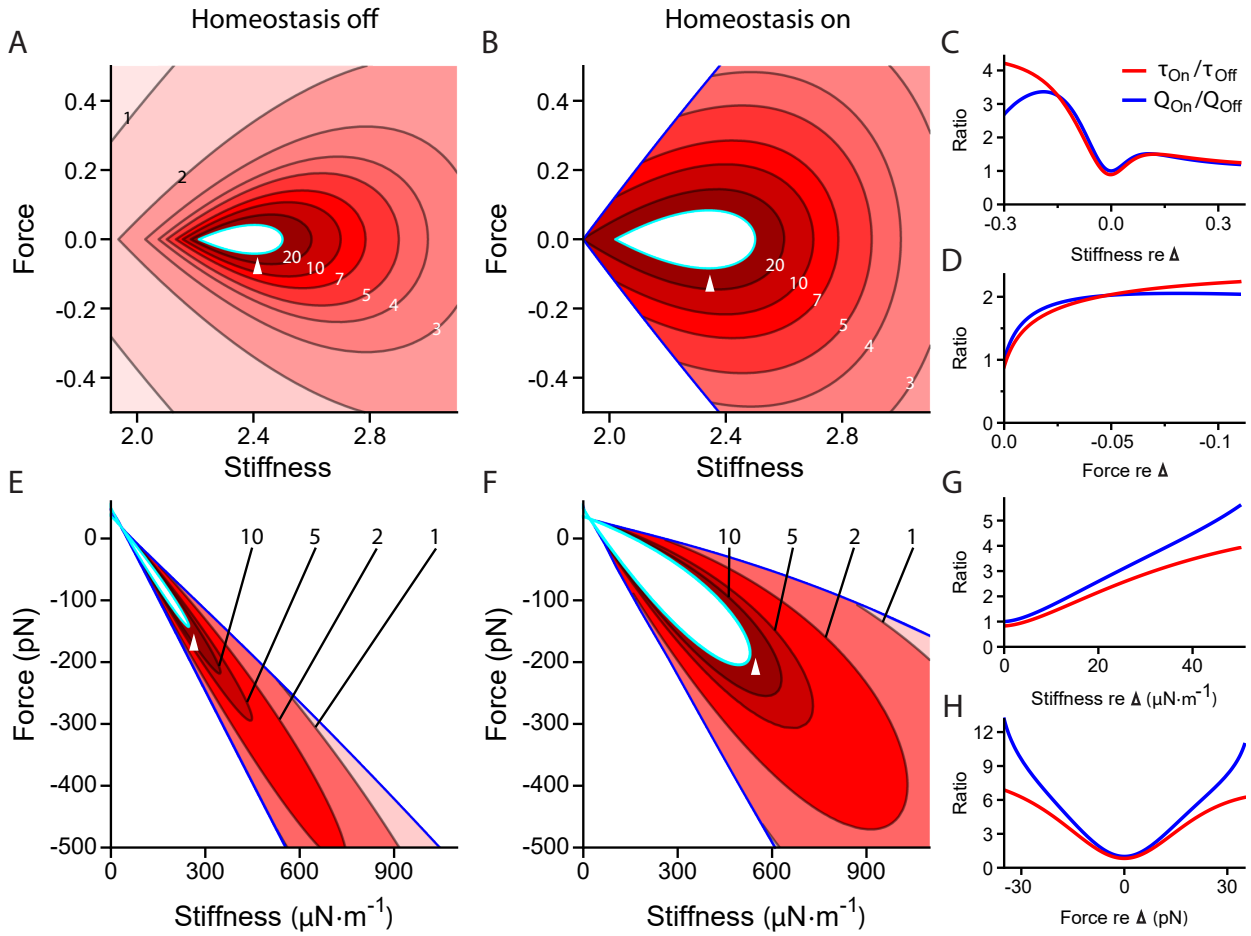

Figure S4. Homeostasis increases the time needed to reach a steady state. (A, B) The time τ, as a function of constant force F_c and stiffness k, for the bundle's response to a small perturbation to decay to $1/e$ times the initial amplitude of the response in Model I when homeostasis is off (A) or on (B). Darker shades of red indicate larger τ values. Contours are labeled by their respective τ values. The Hopf bifurcation curve is colored cyan and the blue curve marks the boundary of the underdamped region. Enhanced robustness of signal detection is achieved through homeostasis by sacrificing how quickly the system can respond to stimuli, as evidenced by the expanded areas enclosed by the τ contours. (C,D) Ratios of τ (red) and quality factor Q (blue) values along horizontal (C) or vertical (D) slices through the reference operating points indicated in panels A and B (apices of the white triangles). The selected slices are the same as in Figure 3. The τ ratio is similar to the Q ratio, illustrating that the enhanced frequency selectivity attained through homeostasis coincides with a slower approach to steady state. $(E-H)$ Same description as panels $A-D$ but for Model II. The τ ratio is less than the Q ratio for Model II, whereas for Model I the τ ratio can exceed the Q ratio, demonstrating that enhanced frequency selectivity can be attained for Model II at a proportionally lower cost in reaction time than for Model I. The contour labels in panels E and F bear units of ms. All parameter values are listed in Tables S1 and S2. Additional bifurcation lines that occur in these regions of the state diagram are not shown (Supplemental Material S8 and S9).

SI Appendix 7: Compressive Range

Calculating the compressive range necessitated simulating each model's response to sinusoidal stimulation spanning a large range of amplitudes at many control parameter values. The driving term $F_0 \cos[\omega_R(k, F_c)\, t]$, in which F_0 is the driving amplitude and the driving frequency is the bundle's resonance frequency $\omega_R(k, F_c)$ at the control parameter values (k, F_c), was added to Eq. 1 or 4 of the main text. Mathematica's `NDSolve` function was then used to numerically solve Eqs. 1 - 3 or 4 - 7 of the main text. A maximum step size of 10^{-3} in Model I and 0.25 μs in Model II was used to ensure faithful reproduction of the nonlinear response; smaller step sizes yielded the same results. Each simulation was allowed to reach steady state, then a long time segment of the simulation was analyzed: in Model I the length of the analyzed segment was 8.5 million steps and in Model II it was 4 million steps or 1 s. These segments contained at least 50 stimulation cycles, and generally many more.

The Fast Fourier transform was applied to the resulting time series, and the peak of the transform's absolute value at the driving frequency was found. The height of this peak divided by the magnitude of the driving force yielded the bundle's sensitivity at that operating point and stimulus amplitude. This procedure was repeated for a set of stimulus amplitudes spanning the ranges depicted in Figure S5. The stimulus amplitudes were logarithmically spaced: each was smaller than the next by a factor of $\sqrt{10}$, except in the regime where the bundle's response transitions from linear to nonlinear, for which the spacing factor was $10^{1/64}$.

A curve of sensitivity *versus* stimulus amplitude, termed a compression curve, was interpolated through splines in doubly logarithmic space from the sensitivity values calculated at each operating point. The bundle's compressive range at this operating point was finally extracted from the bundle's compression curve, as described below. Spline interpolation over the compressive-range values calculated on a grid of points in a state diagram yielded the plots shown in Figure 5.

Compressive range is defined to be the range of driving-force amplitudes over which the slope of the sensitivity compression curve lies between -1 and -1/2 (Figure S5). Model I's homeostatic mechanism employs a non-saturating nonlinearity whereas the nonlinearity in Model II's homeostatic mechanism is saturating. This difference has two important consequences for the compressive range of Model I. First, the compressive range does not possess an intrinsic upper bound. A value of 1 was chosen so that the compressive range in Model I was comparable to that of Model II. Second, when homeostasis is active in Model I, the system is

unstable for very large forcing amplitudes. When x is large, α becomes negative. If $\alpha < 0$ and $y > bx$, y grows exponentially quickly, which in turn causes x to grow rapidly. Choosing the maximum driving force amplitude to be 1 ensures that the unphysical situation of $\alpha < 0$ is avoided.

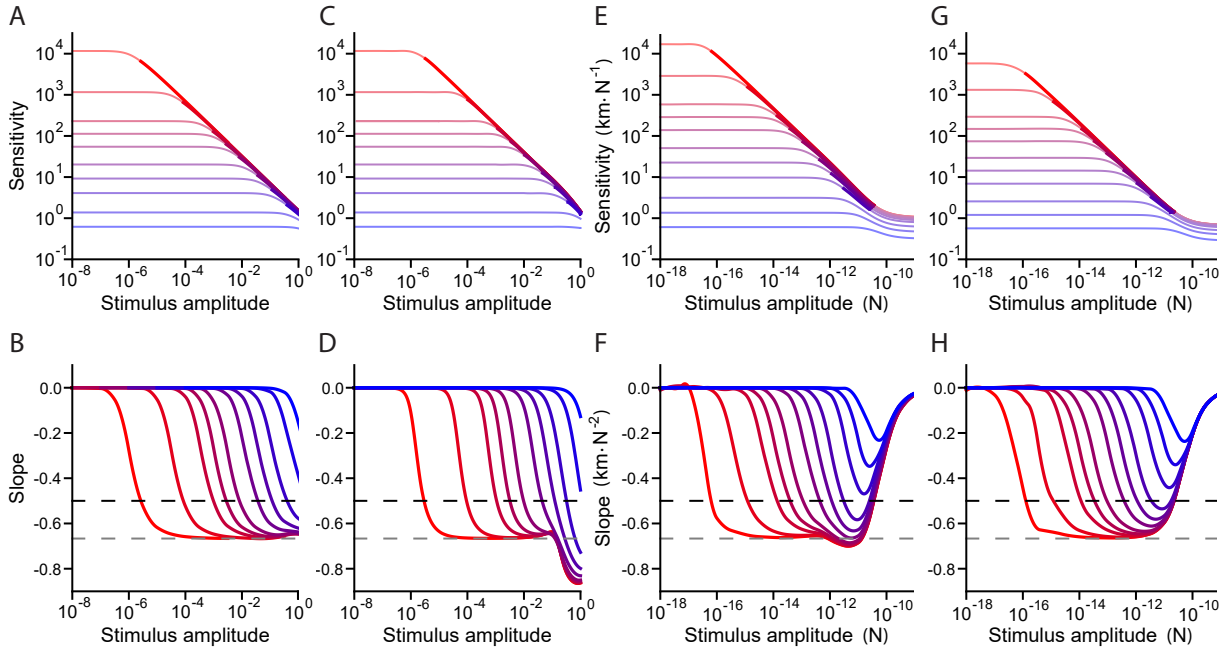

Figure S5. Compression curves. (A, C, E, G) Sensitivity as a function of the amplitude of driving in Model I when homeostasis is either off (A) or on (C), and in Model II in the absence (E) or presence (G) of the homeostatic mechanism. From red to blue, the compression curves were generated at operating points located progressively farther away from the oscillatory region. The bundle's response is linearly related to the stimulus amplitude when the compression curves are flat, whereas a negative slope indicates nonlinear compression. Compression curves are thicker when their slopes lie in the interval (-1,-1/2], or $\chi(F) \sim F^{\epsilon}$, in which -1 $< \epsilon \leq$ -1/2. The slope of each compression curve in panels A, C, E, and G is shown in panels B, D, F, and H, respectively. The dashed black lines in panels B, D, F, and H marks a slope of -1/2 and a slope of -2/3 is indicated by the dashed gray lines. $(A$-$D)$ Curves obtained at $F_c = 0$. $(E$-$H)$ The curves in panels E-F were generated at operating points that fell on the line in which $P_o^* = 0.35$ and $P_o^* = 0.5$ in panels G-H. Curves of the same color correspond to operating points whose Jacobian matrices possess complex eigenvalues with the same real parts. The upper bound on the stimulus amplitude was 1 for all compressive range calculations in Model I.

SI Appendix 8: Excluded Regions

Regions of the state diagram in which multiple stable manifolds coexist were excluded from the compressive-range calculations. Sinusoidal forcing in these regions causes the bundle to jump back and forth between stable manifolds so that the amplitude of the bundle's motion is not well-defined.

The bundle is bistable in a region where two stable fixed points coexist, termed the bistable region. This region is bordered by a curve of saddle node bifurcations, which occur when $\det[J(\vec{a}_*)] = 0$. Equations for these bifurcation curves are given below. The two stable fixed points correspond to two equilibrium positions, one in which the bundle is deflected by a lesser amount and a second where the bundle's deflection is larger. The bistable region is divided into lower and upper parts by the line $F_c = 0$ in Model I and by $P_o^* = 1/2$

in Model II. The sensitivity and quality factor for the lower half of the bistable region were calculated at the equilibrium position corresponding to lesser deflection, whereas the equilibrium position corresponding to greater bundle deflection was employed in the upper half of the bistable region.

A stable fixed point coexists with a stable limit cycle within a region, termed the coexistence region, wedged between a saddle node of limit cycles (SNLC) bifurcation curve and a subcritical Hopf bifurcation curve. These two curves collide with each other and a supercritical Hopf bifurcation curve at a Bautin point. A coexistence region is present in Model II whether homeostasis is on or off. In Model I, however, a coexistence region exists when $\beta_\alpha = 0$ but is absent when $\beta_\alpha = 3/4$ (Figures S6 and S7). Bautin points for both models were found as in (7) and SNLC-bifurcation curves were calculated numerically. Finally, when homeostasis is active in Model I, a region exists in which the bundle exhibits multimodal oscillations in response to periodic forcing. The sensitivity and quality factor for the linearized system were calculated in the coexistence and multimodal-oscillation regions at the stable fixed point in each case.

The condition $\det[J(\vec{a}_*)] = 0$ identifies both saddle node and transcitical bifurcations. In Model I, curves along which these bifurcations occur are given by

$$F_{c,\mathrm{SN}}(k) = \pm\left[(k - a(1-b))\left(\frac{a(1-b)-k}{3(1-b)^3}\right)^{1/2} + (1-b)^3\left(\frac{a(1-b)-k}{3(1-b)^3}\right)^{3/2}\right], \tag{36}$$

$$F_{c,\mathrm{TC}}(k) = \pm\sqrt{\frac{\alpha_0}{\beta_\alpha}}\left[k - a(1-b) + (1-b)^3\frac{\alpha_0^2}{\beta_\alpha^2}\right], \text{ when } \beta_\alpha \neq 0. \tag{37}$$

At $F_{c,\mathrm{SN}}(k)$ the number of x_* solutions abruptly changes from 1 to 3, whereas at $F_{c,\mathrm{TC}}(k)$ two equilibrium points pass through each other and exchange stability. When $\beta_\alpha < 3(1-b)^2\alpha_0/a$ the Hopf bifurcation curve terminates when it intersects $F_{c,\mathrm{SN}}(k)$ at the Bogdanov-Takens points

$$\left(k_{\mathrm{BT}}, F_{c,\mathrm{BT}}\right) = \left\{\frac{3\alpha_0(1-b)^3 - a\beta_\alpha(1-b)}{3b(1-b)^2 - \beta_\alpha}, \pm 2(1-b)^3\left(\frac{ab-\alpha_0}{3b(1-b)^2-\beta_\alpha}\right)^{3/2}\right\}. \tag{38}$$

When $\beta_\alpha > 3(1-b)^2\alpha_0/a$ the Bogdanov-Takens points occur at

$$\left(k_{\mathrm{BT}}, F_{c,\mathrm{BT}}\right) = \left\{a - 3\frac{\alpha_0}{\beta_\alpha}(1-b)^2, \pm\left[ab\sqrt{\frac{\alpha_0}{\beta_\alpha}} - \left(\frac{\alpha_0}{\beta_\alpha}\right)^{3/2}(b^3 - 3b + 1)\right]\right\}, \tag{39}$$

where the Hopf bifurcation curve intersects with $F_{c,\mathrm{TC}}(k)$. Additional bifurcations are accessible when α is zero or negative, conditions that are unphysical. These additional bifurcations are discussed at the end of this document.

The Hopf frequency is

$$\omega_{\mathrm{H}} = \sqrt{\frac{[3(1-b)^2\alpha_0 + (k-a)\beta_\alpha][3(1-b)^2(bk - \alpha_0(1-b)) + \beta_\alpha(k - a(1-b))]}{(3(1-b)^2 - \beta_\alpha)^2}}. \tag{40}$$

$\omega_{\mathrm{H}} = 0$ if $k = k_{\mathrm{BT}}$. When $\beta_\alpha < 3\alpha_0 b(1-b)^2/(2\alpha_0 - ab)$, ω_{H} increases monotonically from 0 at $k = k_{\mathrm{BT}}$ to $\sqrt{\alpha_0(\alpha_0 - ab)}$ at $k = a - \alpha_0$. Otherwise, ω_{H} achieves a maximum value of

$$\omega_{\mathrm{H,max}} = \frac{b}{2}\sqrt{\frac{[a\beta_\alpha - 3\alpha_0(1-b)^2]^2}{\beta_\alpha[\beta_\alpha - 3(1-b)^2]}} \tag{41}$$

$$\text{at } k = \frac{a(2-b)\beta_\alpha^2 - 3(1-b)^2(ab + (2-b)\alpha_0)\beta_\alpha + 9\alpha_0 b(1-b)^4}{2\beta_\alpha^2 - 6b(1-b)^2\beta_\alpha},$$

which is the largest value of k at which a Hopf bifurcation occurs. Detailed state diagrams for Model I are shown in Figure S6. Determining all global bifurcations is beyond the scope of this work.

In Model II, a saddle node bifurcation curve is described by

$$k_{\mathrm{SN}}(P_o^*) = \frac{k_{\mathrm{es}}k_{\mathrm{gs}}[DP_o^*(1-P_o^*) - \delta]}{P_o^*(1-P_o^*)[f_0 S + \beta_f - 2P_o^* S\beta_f - Dk_{\mathrm{gs}}] + \delta(k_{\mathrm{es}} + k_{\mathrm{gs}})}, \tag{42}$$

$$F_{c,\mathrm{SN}}(P_o^*) = \frac{1}{\delta}\ln\left[\frac{AP_o^*}{1-P_o^*}\right]\left(k_{\mathrm{gs}} - k_{\mathrm{SN}}(P_o^*)\left(1 + \frac{k_{\mathrm{gs}}}{k_{\mathrm{es}}}\right)\right) + k_{\mathrm{SN}}(P_o^*)\left(\frac{k_{\mathrm{gs}}}{k_{\mathrm{es}}}DP_o^* - x_{\mathrm{es}} + \frac{1}{k_{\mathrm{es}}}(f_0 - \beta_f P_o^*)(1 - SP_o^*)\right) - k_{\mathrm{gs}}DP_o^*. \tag{43}$$

Bogdanov-Takens points can be found for Model II numerically either from the $T_2 = T_1^2$ condition or by equating the components of $\big(k_{\mathrm{H}}(P_o^*), F_{c,\mathrm{H}}(P_o^*)\big)$ with those of $\big(k_{\mathrm{SN}}(P_o^*), F_{c,\mathrm{SN}}(P_o^*)\big)$.

An analytical expression exists for the Hopf frequency in Model II, but is omitted here to conserve space. Using the parameter values given in Table S2, ω_{H} reaches a maximum value of 136 Hz when homeostasis is inactive ($\beta_f = 0$) and 169 Hz when homeostasis is active. These maximum values occur when $P_o^* \approx 1/2$ in both cases, which corresponds to the point $\big(k_{\mathrm{H}}(1/2), F_{c,\mathrm{H}}(1/2)\big)$ in state space. Detailed state diagrams for Model II are shown in Figure S7.

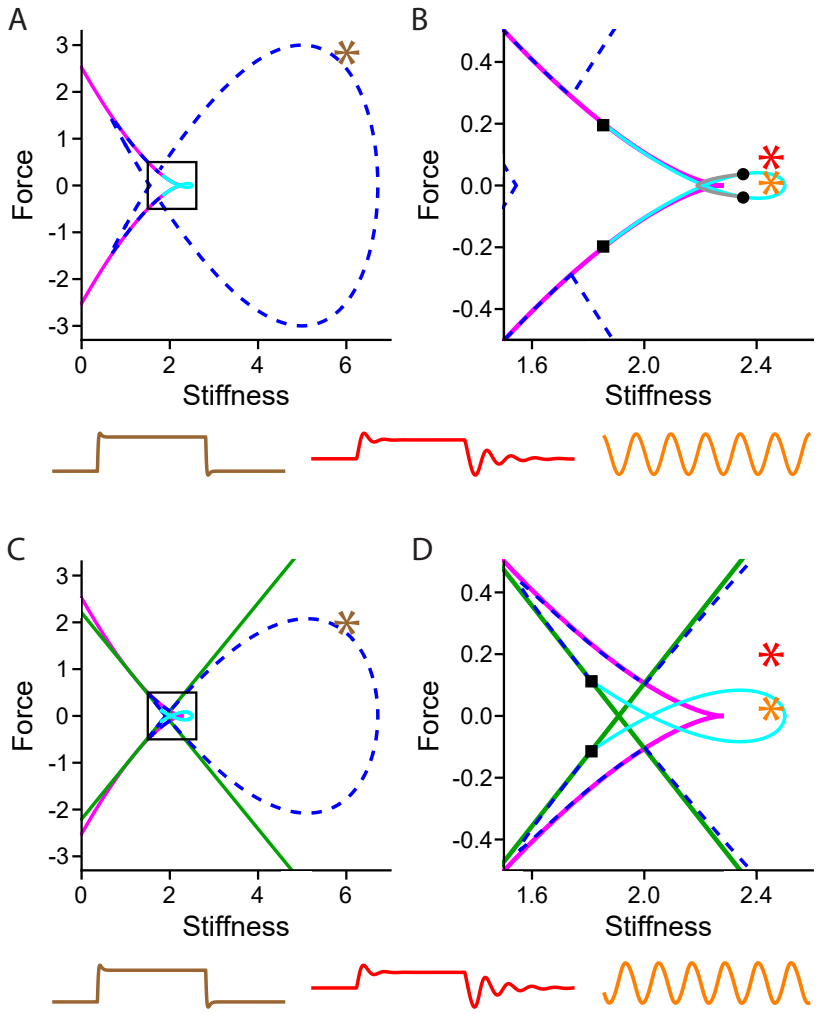

Figure S6. Detailed state diagrams for Model I. State diagrams when homeostasis is either inactive (A,B) or active (C,D). In all panels, the blue dashed curves bound the underdamped region, Hopf bifurcation curves are colored cyan, and saddle-node bifurcation curves are magenta. (A,C) The entire underdamped region is shown. The brown traces depict the hair bundle's response to a force step when the bundle is poised at the operating point marked by brown asterisks. At these operating points the bundle does not exhibit any ringing in response to a force step. (B,D) Magnified view of the region enclosed by the box in panel A (B) or in panel C (D). Bogdanov-Takens points are marked by black squares. When homeostasis is inactive, the bundle's state diagram possesses a saddle node bifurcation of limit cycles (SNLC bifurcation) curve, shown in gray, and Bautin points indicated by black circles. When the homeostasis strength parameter is set to $\beta_\alpha = 3/4$, the model's state diagram lacks Bautin points and SNLC bifurcations, but possesses transcritical bifurcations that are colored green in panels C and D. The red traces, obtained at the operating points marked by red asterisks, depict ringing in the hair bundle's response to a force step. Simulating the behavior of a bundle poised at the operating points marked with orange asterisks yields the orange traces, which confirm that the model exhibits spontaneous oscillations at operating points within the Hopf bifurcation curve. Bautin points were calculated as in (7). The SNLC-bifurcation curve was found numerically.

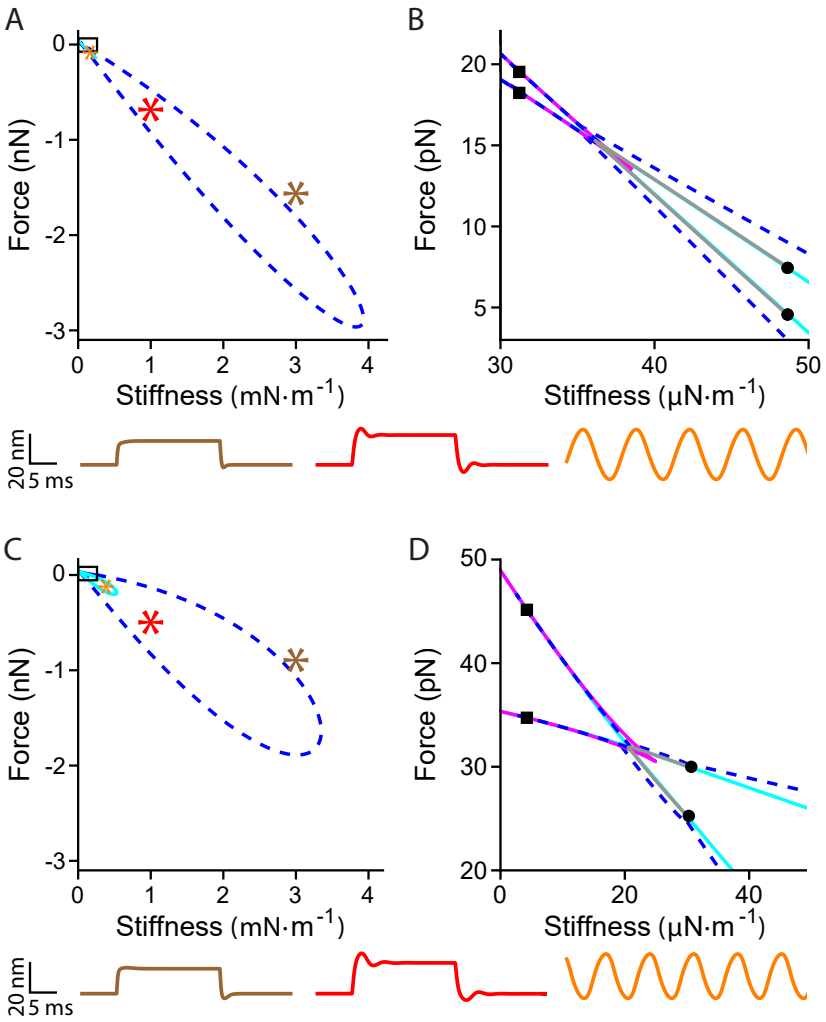

Figure S7. Detailed state diagrams in Model II. State diagrams when homeostasis is either inactive (A,B) or active (C,D). In all panels, the blue dashed curves bound the underdamped region, Hopf bifurcation curves are colored cyan, and saddle-node bifurcation curves are magenta. (A,C) The entire underdamped region is shown. The brown traces depict the hair bundle's response to a force step when the bundle is poised at the operating point marked by brown asterisks. At these operating points the bundle does not exhibit any ringing in response to a force step. Red traces, obtained at the operating points marked by the red asterisks, depict ringing in the hair bundle's response to a force step. Simulating the behavior of a bundle poised at the operating points marked with an orange asterisk yields the orange traces, confirming that the model exhibits spontaneous oscillations at operating points within the Hopf bifurcation curve. (B,D) Magnified view of the region enclosed by the box in panel A (B) or in panel C (D). Bogdanov-Takens points are marked by black squares, Bautin points by black circles, and SNLC-bifurcation curves are colored gray.

SI Appendix 9: Additional Bifurcations in Model I

So far we have assumed that α^*, the inverse of the adaptation timescale in Model I, is greater than zero. Setting $\alpha^* = 0$ inhibits adaptation by rendering it infinitely slow. Although this work does not consider such a scenario, the foregoing discussion is included to give a more complete description of the local bifurcations present in Model I.

Letting $\alpha^* = 0$, we find the following fixed points:

$$\begin{cases} \alpha_* = 0 \\ x_* = \pm\sqrt{\alpha_0/\beta_\alpha} \\ F_c = \pm k\sqrt{\alpha_0/\beta_\alpha} - a(\pm\sqrt{\alpha_0/\beta_\alpha} - f^*) + (\pm\sqrt{\alpha_0/\beta_\alpha} - f_*)^3. \end{cases}$$

These fixed points give rise to two transcritical-bifurcation curves and four saddle node-bifurcation curves:

$$F_{c,\mathrm{TC}\pm}(k) = \pm\sqrt{\frac{\alpha_0}{\beta_\alpha}}\left[k - a(1-b) + \frac{\alpha_0}{\beta_\alpha}(1-b)^3\right], \tag{44}$$

$$F_{c,\mathrm{SN}+}(k) = \pm 2\left(\frac{a}{3}\right)^{3/2} + \sqrt{\frac{\alpha_0}{\beta_\alpha}}, \tag{45}$$

$$F_{c,\mathrm{SN}-}(k) = \pm 2\left(\frac{a}{3}\right)^{3/2} - \sqrt{\frac{\alpha_0}{\beta_\alpha}}. \tag{46}$$

The expressions $F_{c,\mathrm{TC}+}(k)$ and $F_{c,\mathrm{SN}+}(k)$ are associated with the equilibrium point in which $x_* = \sqrt{\alpha_0/\beta_\alpha}$, and $F_{c,\mathrm{TC}-}(k)$ and $F_{c,\mathrm{SN}-}(k)$ with $x_* = -\sqrt{\alpha_0/\beta_\alpha}$. We also find the following Hopf bifurcation curves:

$$k_{\mathrm{H}+}(f_*) = -3\frac{\alpha_0}{\beta_\alpha} - \frac{1}{2\tau_\alpha} + a - 3f_*^2 + 6f_*\sqrt{\frac{\alpha_0}{\beta_\alpha}} + \frac{1}{2\beta_\alpha}\sqrt{2\alpha_0\left[3f_*^2(2+b) + ab + \frac{3b\alpha_0}{\beta_\alpha}\right] - 2f_*\sqrt{\frac{\alpha_0}{\beta_\alpha}}\left[3\alpha_0(1+2b) - a\beta_\alpha + 3f_*^2\beta_\alpha\right]} \tag{47}$$

$$F_{c,\mathrm{H}}(f_*) = k_{\mathrm{H}+}(f_*)\sqrt{\alpha_0/\beta_\alpha} - a(\sqrt{\alpha_0/\beta_\alpha} - f^*) + (\sqrt{\alpha_0/\beta_\alpha} - f_*)^3, \tag{48}$$

when $\alpha_* = 0$, $x_* = \sqrt{\alpha_0/\beta_\alpha}$, and $b\sqrt{\alpha_0/\beta_\alpha} \le f_* \le \sqrt{a/3} + \sqrt{\alpha_0/\beta_\alpha}$, and

$$k_{\mathrm{H}-}(f_*) = -3\frac{\alpha_0}{\beta_\alpha} - \frac{1}{2\tau_\alpha} + a - 3f_*^2 - 6f_*\sqrt{\frac{\alpha_0}{\beta_\alpha}} + \frac{1}{2\beta_\alpha}\sqrt{2\alpha_0\left[3f_*^2(2+b) - ab + \frac{3b\alpha_0}{\beta_\alpha}\right] + 2f_*\sqrt{\frac{\alpha_0}{\beta_\alpha}}\left[3\alpha_0(1+2b) - a\beta_\alpha + 3f_*^2\beta_\alpha\right]} \tag{49}$$

$$F_{c,\mathrm{H}}(f_*) = -k_{\mathrm{H}-}(f_*)\sqrt{\alpha_0/\beta_\alpha} + a(\sqrt{\alpha_0/\beta_\alpha} + f^*) - (\sqrt{\alpha_0/\beta_\alpha} + f_*)^3, \tag{50}$$

when $\alpha_* = 0$, $x_* = -\sqrt{\alpha_0/\beta_\alpha}$, and $-\sqrt{a/3} - \sqrt{\alpha_0/\beta_\alpha} \le f_* \le -b\sqrt{\alpha_0/\beta_\alpha}$.

All of the fixed points in Model I are given by the following three equations:

$$F_c = kf_*/b - af_*(1/b - 1) + f_*(1/b - 1)^3,$$

$$F_c = k\sqrt{\alpha_0/\beta_\alpha} - a(\sqrt{\alpha_0/\beta_\alpha} - f^*) + (\sqrt{\alpha_0/\beta_\alpha} - f_*)^3,$$

$$F_c = -k\sqrt{\alpha_0/\beta_\alpha} + a\sqrt{\alpha_0/\beta_\alpha} + f^*) - (\sqrt{\alpha_0/\beta_\alpha} + f_*)^3.$$

Because the manifolds above are represented by cubic equations, each can contribute from one to three fixed points. Any region of the state diagram therefore contains between three and nine fixed points. The number of stable fixed points in each part of the state diagram is shown in Figure S8 together with the local bifurcations present in Model I.

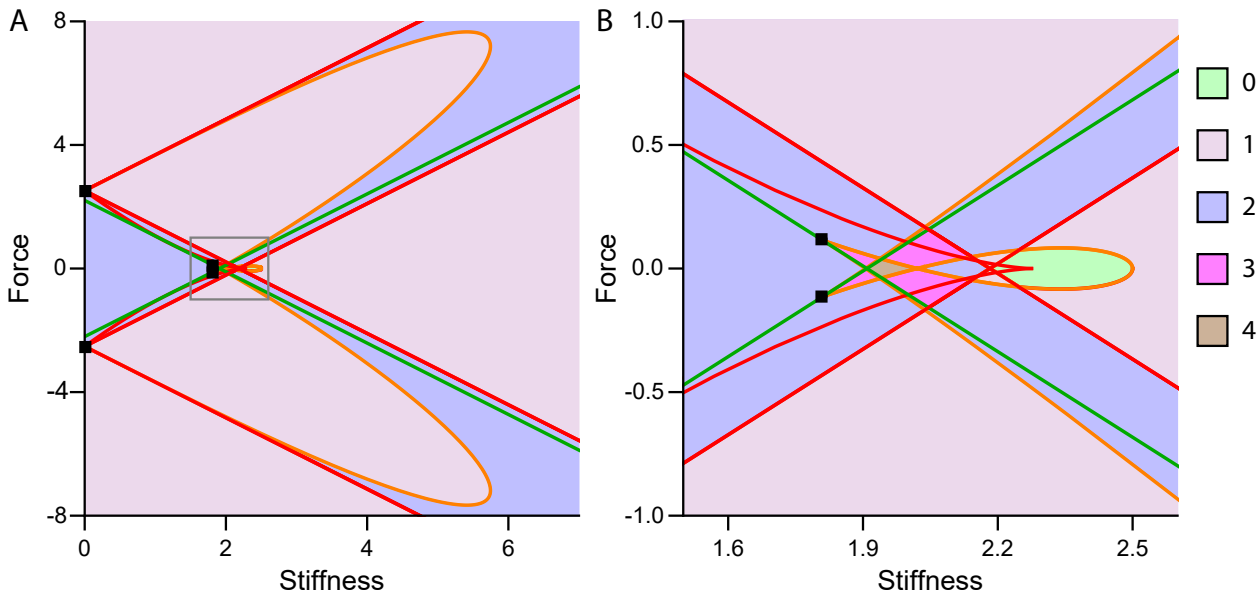

Figure S8. Local bifurcations and stable fixed points in Model I, when $\alpha_* = 0$. (A) Homeostasis is on. (B) A magnified view of the area enclosed by the gray box in panel A. In both panels Hopf bifurcation curves are colored orange, saddle node bifurcation curves are red, and transcritical-bifurcation curves are green. The color with which each part of the state diagram is shaded indicates the number of stable fixed points that reside there.

References for SI Appendix

[1] Hartigan JA, Hartigan PM (1985) The dip test of unimodality. *Ann Stat*, 13(1):70-84

[2] Salvi JD, Ó Maoiléidigh D, Fabella BA, Tobin M, Hudspeth AJ (2015) Control of a hair bundle's mechanosensory function by its mechanical load. *Proc Natl Acad Sci U S A* 112(9):E1000-E1009

[3] Salvi JD, Ó Maoiléidigh D, Hudspeth AJ (2016) Identification of bifurcations from observations of noisy biological oscillators. *Biophys J* 111(4):798-812

[4] Strogatz S (1994) *Nonlinear Dynamics and Chaos* (Addison-Wesley, Reading, MA)

[5] Ó Maoiléidigh D, Nicola EM, Hudspeth AJ (2012) The diverse effects of mechanical loading on active hair bundles. *Proc Natl Acad Sci U S A* 109(6):1943-1948

[6] Nadrowski B, Martin P, Jülicher F (2004) Active hair-bundle motility harnesses noise to operate near an optimum of mechanosensitivity. *Proc Natl Acad Sci U S A* 101(33):12195-12200

[7] Kuznetsov YA (1998) *Elements of Applied Bifurcation Theory* (Springer-Verlag, NY), 2nd edition